Lab on a Chip

PAPER

View Article Online
View Journal | View Issue

Cite this: *Lab Chip*, 2016, **16**, 3374

Real-time assessment of nanoparticle-mediated antigen delivery and cell response†

Carlota A. Cunha-Matos,[a] Owain R. Millington,[b] Alastair W. Wark[c] and Michele Zagnoni*[d]

Nanomaterials are increasingly being developed for applications in biotechnology, including the delivery of therapeutic drugs and of vaccine antigens. However, there is a lack of screening systems that can rapidly assess the dynamics of nanoparticle uptake and their consequential effects on cells. Established *in vitro* approaches are often carried out on a single time point, rely on time-consuming bulk measurements and are based primarily on populations of cell lines. As such, these procedures provide averaged results, do not guarantee precise control over the delivery of nanoparticles to cells and cannot easily generate information about the dynamics of nanoparticle–cell interactions and/or nanoparticle-mediated compound delivery. Combining microfluidics and nanotechnology with imaging techniques, we present a microfluidic platform to monitor nanoparticle uptake and intracellular processing in real-time and at the single-cell level. As proof-of-concept application, the potential of such a system for understanding nanovaccine delivery and processing was investigated and we demonstrate controlled delivery of ovalbumin-conjugated gold nanorods to primary dendritic cells. Using time-lapse microscopy, our approach allowed monitoring of uptake and processing of nanoparticles across a range of concentrations over several hours on hundreds of single-cells. This system represents a novel application of single-cell microfluidics for nanomaterial screening, providing a general platform for studying the dynamics of cell–nanomaterial interactions and representing a cost-saving and time-effective screening tool for many nanomaterial formulations and cell types.

Received 5th May 2016,
Accepted 15th July 2016

DOI: 10.1039/c6lc00599c

www.rsc.org/loc

Introduction

Nanomedicine is a rapidly emerging and promising field for diagnostic and therapeutic applications.[1–3] Central to the effective development of nanoparticles (*e.g.* polymeric, lipidic, and inorganic) for such purposes is the ability to systematically explore how particle properties and environmental factors influence cellular uptake mechanisms, intracellular processing, compound delivery, and inherent toxicity.[1,4] However, standard procedures for testing nanomaterials are often based on end-point measurements and studies are generally limited to a narrow range of parameters (*e.g.* a specific cell type or nanomaterial formulation), making it difficult to achieve global conclusions.[4–7] Additionally, information on the dynamics of nanoparticle uptake and subsequent cellular processing is of utmost importance when investigating cell responses, as the complexity of cell function is dictated by underlying dynamic processes[8] and uptake pathways can strongly influence functional outcomes.[9,10] This highlights the need to develop technological tools that can enable evaluation of cell–nanoparticle interactions with the appropriate temporal and spatial resolutions.

Lab-on-a-chip and microfluidic technologies offer such opportunities,[6,7,11–15] minimising sample volumes and maximising control over the manipulation of particles suspended in laminar flows. Organ,[16] tumour[17,18] and body-on-a-chip[19] studies have shown the importance of producing physiologically relevant microenvironments when testing nanomaterials with respect to static flow well-plate systems, while single-cell microfluidic approaches provide data from a single device with a throughput comparable to that of standard flow cytometry.[20–23] Additionally, microfluidic techniques are compatible with live cell microscopy and can facilitate nanoparticle tracking with intracellular resolution, therefore providing information on the effect of nanomaterials at the single-cell level[6,7,12] and insight into the heterogeneity of responses to nanomaterials.[24,25]

[a] *Department of Biomedical Engineering, University of Strathclyde, 106 Rottenrow, Glasgow, G4 0NW, UK*
[b] *Centre for Biophotonics, Strathclyde Institute of Pharmacy and Biomedical Sciences, University of Strathclyde, 161 Cathedral Street, Glasgow, G4 0RE, UK*
[c] *Centre for Molecular Nanometrology, WestCHEM, Department of Pure and Applied Chemistry, Technology and Innovation Centre, University of Strathclyde, 99 George St, Glasgow, G1 1RD, UK*
[d] *Centre for Microsystems and Photonics, Electronic and Electrical Engineering, University of Strathclyde, 204 George Street, Glasgow, G1 1XW, UK.*
E-mail: michele.zagnoni@strath.ac.uk

† Electronic supplementary information (ESI) available. See DOI: 10.1039/c6lc00599c

One application benefiting from such an approach is the assessment of antigen delivery to dendritic cells.[26] Dendritic cells are a privileged target for vaccine delivery due to their role in the initiation of the immune response through antigen internalization, processing and presentation to lymphocytes.[26–28] Gold nanoparticles have great potential as vaccine carriers due to their biocompatibility and potent adjuvant ability[29,30] and successful targeting to dendritic cells may allow for increased activation at lower antigen dose, potentially reducing side-effects and vaccine production costs.[26,29,31] Additionally, anisotropic particles (such as gold nanorods) have extremely versatile optical properties which can be tuned for specific applications, originating highly specific and stable substrates for intracellular multimodal imaging with sensitivities at the single nanoparticle level.[32,33] To date, microfluidics has shown great promise for providing tools to investigate immunological functions,[34] from cell migration[35,36] to lymphocyte function[37,38] and cell pairing.[39] As new nanomaterials emerge for a variety of immune-based applications, there is a growing need for microfluidic tools that enable the assessment of the dynamics involved in the intracellular processing of antigen *via* nanoparticle-mediated delivery.[6,26,28]

Taking nanoparticle-mediated antigen delivery as a proof-of-concept application, a microfluidic platform was developed to monitor in real-time hundreds of primary, murine bone marrow-derived dendritic cells at the single-cell level following exposure to a range of concentrations of ovalbumin-conjugated gold nanorods. Time-lapse microscopy enabled specific aspects of cell function to be monitored: nanoparticle uptake was proportional to the fluorescence intensity of a dye encapsulated in the nanorods, while antigen processing was identified by intracellular enzymatic cleavage of ovalbumin-conjugated fluorophores. This novel combination of single-cell microfluidics with customised nanorods and imaging techniques for nano-vaccine screening yielded outcomes that provide unique information regarding the dynamics of nanoparticle/single-cell interactions and nanoparticle-mediated antigen delivery.

Experimental protocols

Preparation and characterisation of gold nanorod conjugates

Synthesis of gold nanorods (NRs) was performed using an adapted version[40,41] of the seed-mediated growth method using cetyltriethylammonium bromide (CTAB),[42,43] followed by fluorescence/Raman reporter dye incorporation[41] and polyelectrolyte wrapping[44] (detailed procedures described in ESI†). The design and optical characterisation of the NR conjugates used in this study are described in Fig. S1.† The developed NRs were biocompatible at the concentrations used (Fig. S1b†) and emitted fluorescence at >650 nm when excited at 633 nm (Fig. S1c†) due to the incorporated reporter dye. The colloidal suspensions of polymer-wrapped NRs were monitored for >6 months with no change in the UV-vis or SERRS properties, indicating very good stability of the CTAB/dye layer following polymer wrapping, as previously described.[32,41] To assess the NR suitability for use in cellular environments, colloidal stability in serum-containing culture medium was tested for nanoparticles with different polyelectrolyte coatings (procedures in ESI†). Following this (Fig. S1e and f†), only the three-layer polymer configuration (PSS-PDDAC-PSS) was used, which ensured colloidal stability in both the cell culture and microfluidic environments.

Preparation and analysis of dendritic cells

Bone marrow-derived dendritic cells were generated from BALB/c or Ly5.1 congenic mice (maintained in accordance with local ethical committee and UK Home Office guidelines) as previously described.[45] After culture for 7–8 days, cells were routinely checked for specific surface phenotype (CD11c) and activation (CD40) markers [eBioscience, UK] using flow cytometry, with typically over 90% of the cells being CD11c positive in the samples used (Fig. S2†). Off-chip testing of NR conjugates for biocompatibility and antigen delivery was performed using the procedures described in ESI.† DQ Ovalbumin (DQOVA) is an ovalbumin conjugate containing a quenched BODIPY fluorescence dye which becomes fluorescent upon cleavage by intracellular proteases, and is thus a good indicator of antigen processing by dendritic cells.[46] Therefore, NR–DQOVA conjugates were produced and tested off-chip with cells, as an initial assessment of the coating procedure and of cell response under different experimental conditions (*i.e.* to optimize the range of concentrations and incubation times) prior to their use in the microfluidic device. Flow cytometry was performed to obtain end-point measurements of cell samples exposed to different concentrations of NR–DQOVA and soluble DQOVA for different periods of time. Confocal microscopy was used to assess internalization of NR–DQOVA conjugates and antigen processing. To assess the functionality of the developed NR conjugates, NRs were conjugated to non-labelled ovalbumin (OVA) and added to dendritic cells and OVA-specific OT-II T cells to assess whether antigen on the NR surface was processed and presented to T cells to initiate an adaptive immune response. T cell activation was measured by CD69 surface marker expression on the surface of CD4+ T cells using flow cytometry, while ELISA was used to assess cytokine (interferon-γ) production.

Cell trapping, nanorod delivery and real-time cell monitoring in the microfluidic device

Microfluidic devices, consisting of three inlets, one outlet and one trap array chamber, were fabricated using standard photo- and soft-lithography procedures, as described in ESI.† For time-lapse imaging, the devices were inserted in a Tokai Hit INUB-WELS-F1 microscope stage incubator [Tokai, Japan] and kept at 37 °C, 5% CO_2 and high humidity conditions for the duration of the experiments. Devices were sequentially primed manually with 70% isopropanol and deionised water

prior to cell injection. Syringe pumps [Aladdin 220, World Precision Instrument, UK] were connected to the device *via* microbore polytetrafluoroethylene (PTFE) tubing [Cole Parmer, UK]. Dendritic cells at 1.5–3 × 10^6 cells per ml in complete RPMI (see ESI†) were withdrawn into the PTFE tubing using a syringe pump, and subsequently loaded into the device at 1.5 μl min^{-1} for at least 2 hours to allow for settling of the cells into a chamber hosting an array of microtraps. After trapping, a suspension of 400 pM (approximate optical density of 2) NR–DQOVA conjugates in complete RPMI was delivered into the trap array at 0.5 μl min^{-1} through one side inlet, whilst the contralateral inlet was used to dispense medium at the same flow rate, forming an adjustable range of NR concentrations across the trap array chamber (Fig. S3†). This flow condition was maintained for 2 h, after which culture medium was continuously perfused through the array of cells for the remaining duration of the experiment at 0.5 μl min^{-1}. Time-lapse bright-field and fluorescence imaging (20× objective – 0.323 μm per pixel, 32 tiles acquired every 5 minutes for 8 hours) covering over a third of the trapping array was performed using an automated Zeiss Axiovert Observer inverted microscope with Colibri 2 LED illumination, AxioCam camera and Zen 2 Pro acquisition software.

Single-cell data analysis

Microscopy images were analysed using Zen 2 Pro software. Circular regions of interest (ROI) were defined around each trapped cell and corrected for position if the cells moved over time, ensuring single-cell data consistency over the course of the experiment. Cells adhering to the outside of the traps were not considered. The mean fluorescence intensity (MFI) for each ROI was then extracted and analysed. For analysis of cell population response with respect to nanoparticle concentration, ROI data was grouped into three regions of the array containing approximately the same number of traps according to the flow conditions: a null NR concentration region, a medium NR concentration region, corresponding to the particle concentration gradient, and a high NR concentration region. Background correction was done using a circular ROI situated outside the traps in the null concentration region and a 5th-degree polynomial curve was used to fit the data.

Results

The microfluidic device consisted of three inlets, a trapping chamber containing an array of 1512 traps, and one outlet (Fig. 1a). One inlet was used to flow a cell suspension into

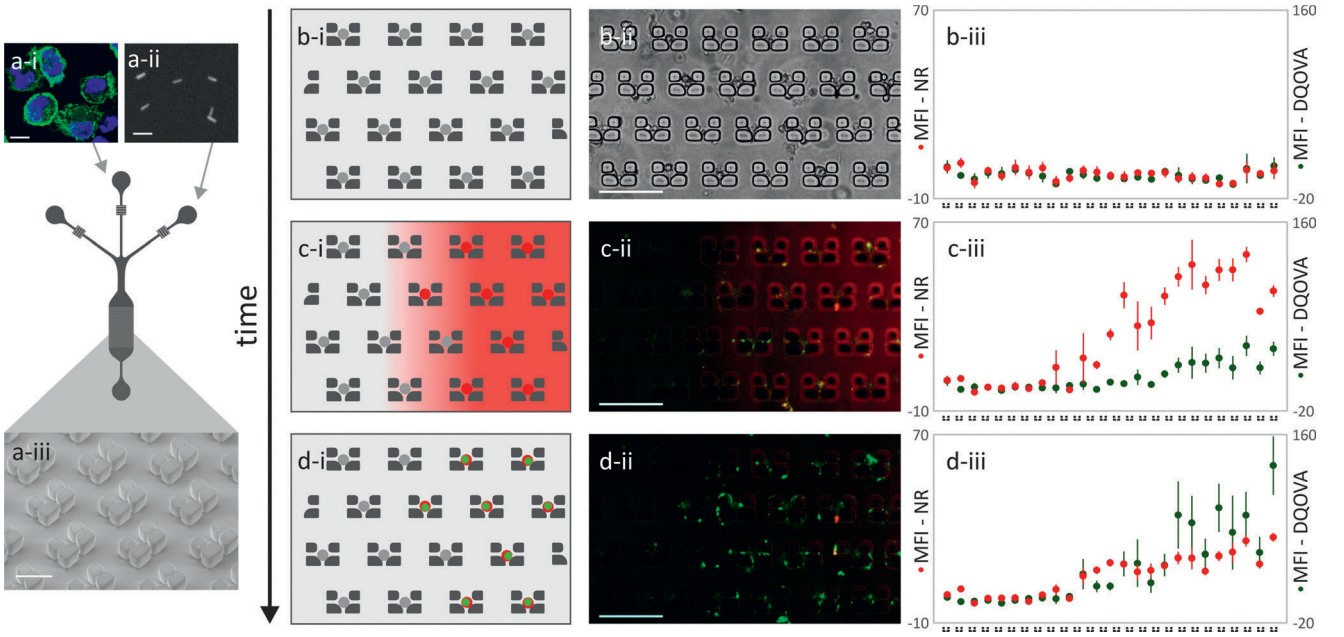

Fig. 1 Schematic representation of the microfluidic system and protocol developed for investigating cell–nanoparticle interactions and real-time antigen processing. (a) Dendritic cells (a-i – confocal fluorescence image of dendritic cells with the membranes stained with cholera-toxin-B (green) and DAPI-stained nucleus (blue). Scale bar = 10 μm) and nanorods (a-ii – SEM image of gold NRs with longitudinal λ_{max} of 765 nm. Scale bar = 100 nm) were sequentially injected into a microfluidic device containing an array of microtraps (a-iii – SEM image of the PDMS microtrap array. Scale bar = 40 μm). (b, c, d-i) Schematic representation of the key temporal aspects of the microfluidic protocol: cell trapping, NR delivery and antigen processing, respectively, from top to bottom. Cells are represented in grey: they become red when in contact with NRs and turn green after antigen processing. (b, c, d-ii) Phase contrast and composite images of the trapping array (scale bar = 100 μm) corresponding to the time points of the schematics in b, c, d-i. (b, c, d-iii) Fluorescence intensity profile showing responses to NR uptake and antigen processing across the width of the array chamber for the time points corresponding to the schematics in b, c, d-i. Each data point represents the mean fluorescence intensity (MFI) (background corrected) of single-cell ROIs located in the same vertical region of the chamber over five rows ± standard error of the mean (S.E.M.), with red representing NR fluorescence measured at 625 nm excitation and green representing DQOVA fluorescence measured at 488 nm excitation.

the trap array chamber while the others were subsequently utilized to produce a NR concentration gradient across the width of the array. Each trap had an inner width of 20 μm and constituted a low shear stress pocket (<0.05 dyn cm^{-2}), thus inducing cell trapping without damaging the cell membrane.[21] The device and protocol developed resulted in the successful trapping of hundreds of dendritic cells at the single-cell level. Typically, for the cell concentration and flow rates used, 17% of the total trap sites remained empty or contained cell debris, 68% contained single-cells and 15% contained 2 or 3 cells. By using primary dendritic cells, a greater variability in cell shape, size and activation status is present with respect to the use of cell lines, which leads to challenges in achieving uniform cell trapping. Overall, considering traps containing between 1 and 3 cells, 83% trapping efficiency was obtained in our system, with all of the trapped cells that could be individually tracked. During injection, cells retained a round shape and, within 15 minutes, displayed characteristic branched projections (or dendrites), thus confirming their viable state. Cells could be cultured in the microfluidics at 37 °C and 5% CO_2 under continuous perfusion in growth medium, with no detectable damage to the cells for up to 24 hours. Viability staining was performed on cells after 24 hours of culture in the trapping chamber and following exposure to NRs. Results (Fig. S4†) show the biocompatible nature of the microfluidic setup, protocols and NRs used.

Following successful cell trapping in the microfluidic array (Fig. 1b), wide-field images of approximately 550 traps were acquired every five minutes over eight hours. Delivery of NR–DQOVA conjugates was initiated 30 minutes after starting time-lapse recording and continued for approximately two hours (Fig. 1c), with the protocol developed resulting in the left side of the array receiving no nanoparticles, the middle area receiving a concentration gradient of nanoparticles and the right side receiving a uniform concentration of nanoparticles (Fig. S3†). Subsequently, perfusion with medium alone was continued until the end of the experiment (Fig. 1d). Phase contrast was used to identify cells in traps, whilst the fluorescent signals corresponding to NR uptake and antigen processing were monitored using the red (625 nm excitation) and green (488 nm excitation) channels, respectively. Fig. 1(b, c, d-iii) shows the average fluorescence intensity profile for single-cells within five rows across the entire width of the array. As expected, during nanoparticle delivery, there was an increase in red fluorescence intensity on the high NR concentration region (right side in Fig. 1c-iii). This was followed by an increase in green fluorescence intensity as the dendritic cells processed the delivered antigen, whilst the NR-deficient area had no detectable fluorescence signal (Fig. 1d-iii). For analysis of the time-dependence of single-cell response, the trap array was divided into three regions containing approximately the same number of traps, according to the level of exposure to different nanoparticle conjugate concentrations. Fig. 2 shows the MFI of all the single-cells in each of these regions, with a peak in red fluorescence (b-i, c-i) marking the highest concentration of NR exposure to the cells, followed by a gradual increase in green fluorescence corresponding to antigen processing as measured by DQOVA cleavage (b-ii, c-ii). These results clearly demonstrate the capacity of our system for monitoring the time- and dose-dependent uptake and processing of antigen-coated nanoparticles in real-time across a population of trapped cells.

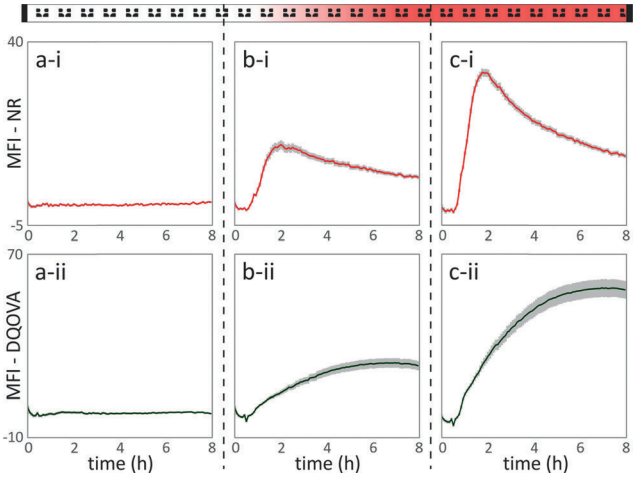

Fig. 2 Representative plots of averaged single-cell responses following nanoparticle uptake and antigen processing. Circular ROIs were drawn around individual cells for data acquired every 5 minutes over 8 hours. For analysis purposes, three regions were defined according to different nanoparticle concentrations: (a) null concentration (N = 151), (b) medium concentration (N = 203) and (c) high concentration (N = 171) regions, as per the illustrated nanoparticle concentration gradient profile (top). Graphs show the response of single-cells in each of these regions. (a, b, c-i) Average NR fluorescence intensity (background corrected) measured at 625 nm excitation ± S.E.M. (a, b, c-ii) Average DQOVA fluorescence intensity (background corrected) measured at 488 nm excitation ± S.E.M.

Following assessment of the population response for different NR–DQOVA concentrations delivered, individual cells were analysed in order to assess cell response heterogeneity, as well as the dynamics of NR uptake and processing at the single-cell level. To do this, heatmaps were produced representing the level of DQOVA processing for all the single-cell ROIs (Fig. 3a, b, c,-i) according to their position in the array, showing clear variability in terms of amount of antigen processed and speed of response. Example of cell heterogeneity in response to antigen delivery is also shown for single-cells in five different traps exposed to the same concentration of NRs (Fig. 4a). Additionally, fluorescent intensity traces of all the individual cells under analysis were extracted and examples are shown for each of the array regions (Fig. 3a, b, c,-ii and iii). Video S1† shows representative time-lapse images for cells in these three regions.

Subsequently, we investigated whether an increasing NR uptake correlated with enhanced antigen-processing. For this analysis, cells were gated as NR+DQOVA+ based on their fluorescence intensities above background level for both channels to identify cells that both took up nanoparticles and

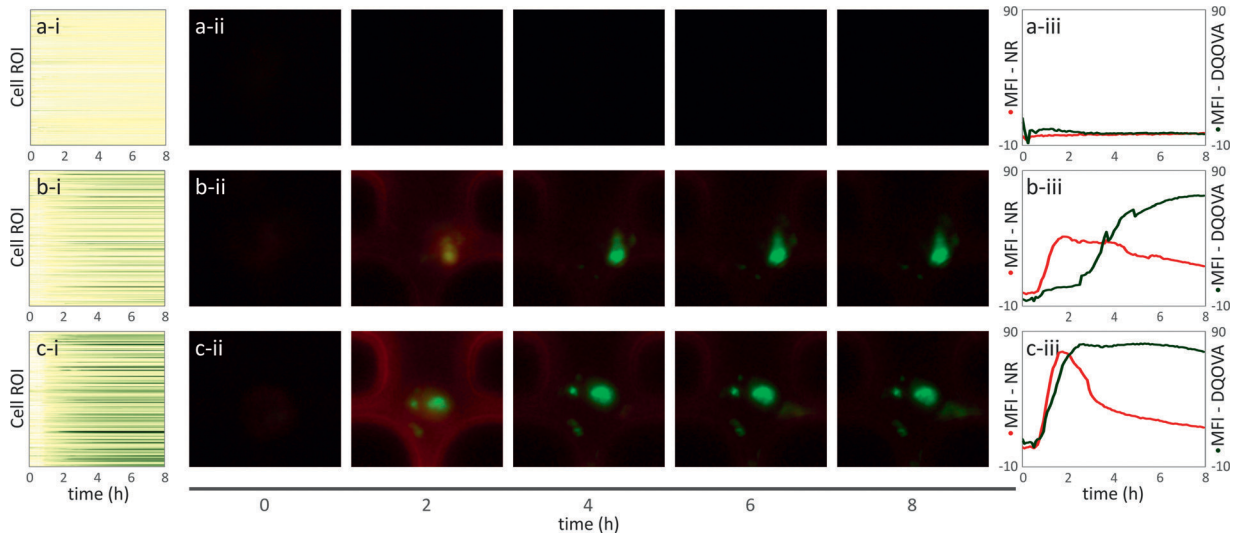

Fig. 3 Comparison of single-cell responses to NR-conjugate delivery in the (a) null, (b) medium and (c) high NR concentration regions of the microfluidic array. (a, b, c-i) Heatmaps showing processing of DQOVA within individual cell ROIs, where white corresponds to a null response and dark green is the maximum MFI value across the whole array, with the midpoint (yellow) at the 50th percentile. Examples of single-cell ROIs were then selected from each area of the microfluidic array and their fluorescence intensity profiles plotted to assess their response patterns. (a, b, c-ii) Composite fluorescence images of trapped cells for different time points over 8 hours and (a, b, c-iii) MFI plots for the same ROIs over 8 hours, where red indicates NR exposure, measured at 625 nm excitation, and green indicates DQOVA processing, measured at 488 nm excitation.

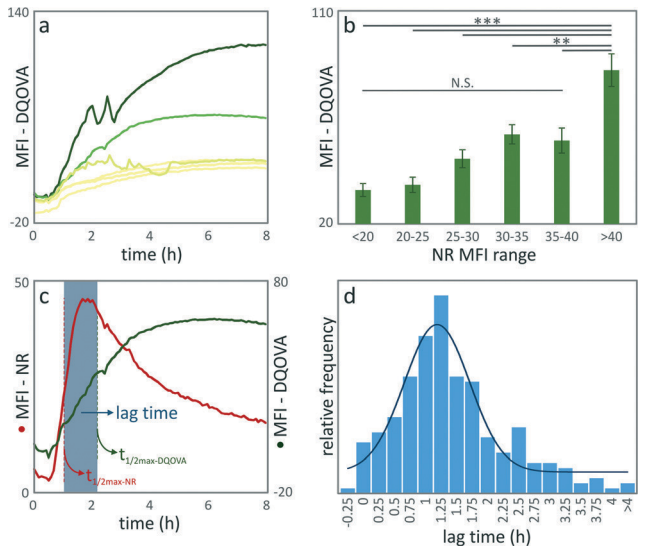

Fig. 4 Analysis of single-cell response to antigen processing. (a) Examples of MFI profiles for DQOVA from six cells in different traps within the high NR concentration region, showing heterogeneous cell response to antigen-coated NRs. Traces are coloured according to intensity as per heatmaps in Fig. 3. (b) Average DQOVA MFI range (max–min) for gated single-cell ROIs depending on NR MFI range (max–min) (±S.E.M.; N between 23 and 61 cells; significant differences determined by one-way analysis of variance test with $^{**}p < 0.01$, $^{***}p < 0.001$). (c) Illustration of the parameters used for measuring the time delay ("lag time") between nanoparticle uptake and antigen processing (MFI traces) for each individual cell ROI, calculated as the time difference between NR half-maximum MFI and DQOVA half-maximum MFI (blue bar). (d) Histogram showing the lag time response for all the gated single-cell ROIs with damped least-squares Gaussian fit (σ = 0.526) superimposed. Single-cell ROIs shown in (b) and (d) were gated as NR+ and DQOVA+.

processed antigen. This double positive population represented 0.6%, 43.3% and 84.3% of total cells in the null, medium and high concentration regions, respectively. Fig. 4b shows the intensity of antigen processing by gated single-cells with different levels of NR uptake. These data suggest that an increased accumulation of NRs in cells correlated with higher processing of DQOVA.

The dynamics of vaccine uptake, processing and presentation can have a key role in determining the magnitude and type of immune response induced. Therefore, we measured the lag time between the peak of NR uptake and antigen processing (Fig. 4c) for all the gated cells. The results (Fig. 4d) indicate that despite being exposed to different concentrations and acquiring different amounts of NR conjugates, the time delay between NR uptake and antigen processing followed a Gaussian distribution, with the standard deviation of the fitted curve (continuous line in Fig. 4d) being representative of response heterogeneity.

While microfluidic techniques have been used to perform lymphocyte activation and cell pairing experiments,[37–39] the scope of this work is to provide a general platform for screening nanoparticle conjugates for nanomedicine research. Therefore, following validation of nanoparticle-mediated delivery of antigen to dendritic cells on-chip, off-chip tests were performed to confirm that the antigen was not only processed (quantified using DQOVA in Fig. 1–4), but also presented to T cells. For this, OVA-specific T cells were allowed to interact with dendritic cells exposed to various concentrations of NR–OVA or OVA only, as described in ESI.† Analysis using flow cytometry (Fig. 5a) showed significantly increased expression of CD69 (suggesting recent activation) on the surface of OVA-specific T cells that were added to

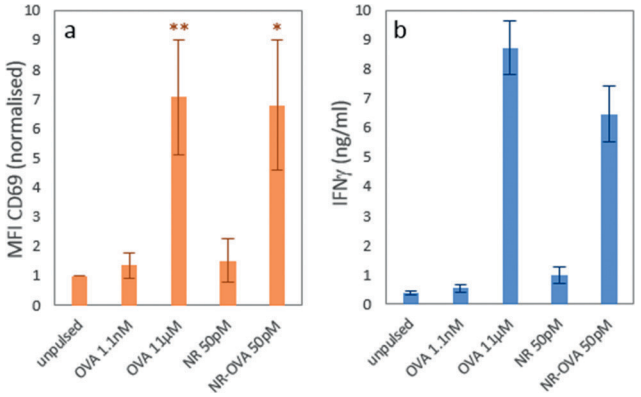

Fig. 5 Assessment of NR-mediated immune response generation compared with soluble ovalbumin. OVA-specific OT-II T cells were incubated with dendritic cells and different NR formulations or soluble OVA for 72 h. (a) Flow cytometry data of CD4+ T cells showing the MFI of CD69 as a measure of lymphocyte activation. Data has been normalised to the unpulsed sample for each separate experiment, for presentation clarity, and results shown are mean value ± S.E.M. of four independent experiments. Significant differences to the unpulsed sample were determined on the absolute MFI values by two-way analysis of variance with Fisher means comparison (*$p < 0.05$, **$p < 0.01$). (b) ELISA data showing cytokine (IFNγ) production by the T cells. Data is mean value ± S.D. of technical duplicates. Results show that NR–OVA conjugates have successfully delivered antigen to the dendritic cells, which was then presented to T cells to initiate an adaptive immune response.

dendritic cells exposed to NR–OVA, over four separate experiments. Additionally, ELISA data (Fig. 5b) showed that the same T cells were actively producing high levels of interferon-γ (IFNγ) after 72 h of co-culture – a cytokine that is only produced by T cells that have been efficiently activated by antigen-presentation. Together, these data demonstrate that the NR–OVA conjugates are efficiently delivered to dendritic cells where they are rapidly processed and NR-associated antigens can be presented to T cells to induce a specific adaptive immune response.

Discussion

In this study, we present a microfluidic platform to monitor the controlled delivery of antigen-conjugated nanoparticles to biologically-relevant, primary dendritic cells, providing a new methodology to investigate the nanoparticle–cell dynamics involved in nanoparticle-mediated antigen delivery in a manner not possible using conventional methods.

We have previously shown that the developed gold NR conjugates provide a highly stable rod-dye combination with very specific and tunable imaging capabilities,[32,41] such as combined surface-enhanced resonance Raman spectroscopy (SERRS) and fluorescence microscopy (Fig. S1b and c†). Here, under the controlled laminar flow conditions provided by microfluidics, we show how fluorescence microscopy can be used to assess nanoparticle uptake without requiring additional fluorescent probes. This highlights the potential of this system to integrate multimodal imaging capabilities. For example, SERRS mapping data was also obtained within the microfluidic device, following a NR concentration gradient in the array (Fig. S5†). Good correlation between the fluorescence and SERRS measurements of nanoparticle uptake indicates that our approach is amenable to applying more than one imaging modality for the real-time monitoring of nanoparticle–cell interactions in the future, along with particle intracellular distribution. For the current application, NRs were further conjugated to DQOVA, an ovalbumin-dye conjugate that becomes fluorescent upon cleavage by intracellular proteases (commonly used as a marker for antigen processing). This allowed for simultaneous tracking of nanovaccine uptake and processing by cells using fluorescence microscopy.

Following successful cell trapping and NR delivery in the microfluidic device, real time NR uptake and antigen processing data was obtained from 525 trapped single-cells over 8 hours, showing the capabilities of the developed microfluidic platform to provide statistically relevant data, as well as single-cell resolution over long periods of time. In this work, approximately 45 000 cells were required for one microfluidic experiment, in comparison with at least 2.4 million cells used to run the equivalent experiments off-chip in well plates and in static conditions. This is especially relevant when dealing with rare or patient-derived cell samples and further highlights the capabilities of the system as a prescreening tool for nanomaterials for clinical applications.

NR delivery was achieved successfully and, in addition to delivering different particle concentrations simultaneously, the microfluidic procedure ensured that NR conjugates were in contact with cells only for a defined amount of time and under constant flow conditions. Using the proposed microfluidic approach, a more controlled particle delivery to cells is obtained with respect to that in equivalent well plate experiments. In fact, in the latter, shortly after particle injection into the wells, NRs sediment at the bottom of the plate and it is reasonable to assume that the degree of nanoparticle uptake by cells will depend mostly on their level of activity or motility within the plate, with the most motile cells internalising nanomaterial at a greater rate than stationary or less motile cells (Video S2†). However, this information cannot be extracted from flow cytometry analysis and presents one of the disadvantages of performing well plate based experiments. Our data shows that the microfluidic approach provided information from a cell population comparable to that obtained with flow cytometry, but allowing for the additional assessment of the cell–nanoparticle interaction dynamics, as opposed to end-point measurements of separate samples. Therefore, the methodology developed here, allowing a controlled amount of NRs to be delivered for a defined period of time, represents a more relevant *in vivo*-like delivery environment than that achieved carrying out experiments in static conditions.[24,47]

Differences in NR conjugate concentration delivered across the array and subsequent differences in antigen processing response could be assessed both at the population

level (Fig. 2) and at the single-cell level (Fig. 3). The heterogeneity of time and intensity of cell response to similar stimuli, as shown in the heatmaps in Fig. 3(a, b, c-i), underlines the importance of acquiring single-cell information to better understand cellular behaviour, as opposed to averaged population responses. Fig. 4a further emphasises the heterogeneity of response by comparing single-cell traces of DQOVA fluorescence for cells in the same NR concentration region. This outcome can be attributed to different degrees of cell activation, leading to either up-regulation or down-regulation of uptake mechanisms, as well as viability status, and its assessment is of vital importance when investigating cellular response to stimuli.[25,39,48] Off-chip confocal imaging showed bright fluorescence of the NR-delivered DQOVA complexes within the intracellular space (Fig. S6†). Interestingly, DQOVA fluorescence was delocalised from the signal obtained from NRs, suggesting the antigen molecules could have detached from the NR surface. Overall, the optical properties of labelled gold NRs combined with the developed microfluidic platform have the potential to provide data on the intracellular processing pathways involved in nanovaccine delivery and subsequent release of antigen from the surface of nanoparticles.

Finally, the use of primary cells, that are heterogeneous in morphology and size, allowed for a more reliable assessment of cell function when compared to work done with cell lines.[49] Specifically, dendritic cells are involved in key aspects of the immune system, internalising pathogens and foreign materials and initiating adaptive immunity through presentation of antigen to T cells. This leads to the stimulation of lymphocyte activation, proliferation and differentiation into effector T cells, which are capable of producing cytokines,[27] outcomes that were validated using additional flow cytometry and ELISA measurements for the developed NR conjugates (Fig. 5). It is worth noting that similar T cell activation profiles were obtained for an estimated concentration of OVA delivered by NR (~1 nM, see Methods in ESI†) that was approximately four orders of magnitude lower than that of soluble OVA used as a positive control (11 μM). No T cell activation was elicited by similar low concentrations (1.1 nM) of soluble OVA. This suggests that the NR formulation used may facilitate antigen uptake as well as having adjuvant activity, consistently with existing evidence that polymer-wrapped gold nanorods can act as powerful adjuvants,[30] a valuable feature for the development of efficient nanovaccines.[29,50,51] On-chip delivery of a concentration gradient of 0–222 nM soluble DQOVA was also tested and provided comparable fluorescent signal to that obtained with the NR concentration gradient using 400 pM NR–DQOVA conjugates (~8 nM DQOVA, Fig. S7†). Overall, when combined with the microfluidics data described above, these results demonstrate the important role that microfluidics can play in the design and efficient optimisation of new nanovaccine formulations, including assessing the dose and uptake kinetics, with the future potential to develop more complex intercellular studies.

Conclusion

This work presents a novel microfluidic approach for studying the dynamics of cell response to nanomaterials. A nanoparticle-antigen model was developed to induce the immune response of primary dendritic cells using a microfluidic platform that provides high-throughput, real-time information on the cellular–nanoparticle interactions. The use of biologically-relevant primary cells has numerous advantages over previous work using cell lines, especially when translating results towards *in vivo* development. With increasing interest in the application of nanotechnology for the delivery of vaccines and therapeutic drugs, the real-time cell monitoring platform presented here can greatly improve the investigation of effects produced by nano-carriers, providing statistically-relevant information about the dynamics of intracellular processes underlying the interaction of cells with different nanomaterial formulations – with applications ranging from the initial biocompatibility testing to enhanced control over molecule delivery (for example, through the use of targeting molecules or pH-dependent delivery systems). Importantly, the presented platform can be easily adapted for use with different cell types and particle formulations, making it a versatile tool for the initial screening and development of nanomaterials for biomedical applications.

Acknowledgements

The authors would like to thank the Engineering and Physical Science Research Council (EPSRC) funding *via* "Bridging the Gap" scheme (EP/J501554/1) and the EPSRC Doctoral Training Centre (DTC) in Medical Devices at the University of Strathclyde (EP/F50036X/1).

References

1 L. K. Bogart, G. Pourroy, C. J. Murphy, V. Puntes, T. Pellegrino, D. Rosenblum, D. Peer and R. Lévy, *ACS Nano*, 2014, **8**, 3107–3122.
2 E. C. Dreaden, A. M. Alkilany, X. Huang, C. J. Murphy and M. A. El-Sayed, *Chem. Soc. Rev.*, 2012, **41**, 2740.
3 L. Zhao, A. Seth, N. Wibowo, C.-X. Zhao, N. Mitter, C. Yu and A. P. J. Middelberg, *Vaccine*, 2014, **32**, 327–337.
4 A. M. Alkilany, L. B. Thompson, S. P. Boulos, P. N. Sisco and C. J. Murphy, *Adv. Drug Delivery Rev.*, 2012, **64**, 190–199.
5 A. M. Alkilany and C. J. Murphy, *J. Nanopart. Res.*, 2010, **12**, 2313–2333.
6 P. Shah, A. Kaushik, X. Zhu, C. Zhang and C.-Z. Li, *Analyst*, 2014, **139**, 2088–2098.
7 V. Giridharan, Y. Yun, P. Hajdu, L. Conforti, B. Collins, Y. Jang and J. Sankar, *J. Nanomater.*, 2012, **2012**, 789841.
8 D. G. Spiller, C. D. Wood, D. A. Rand and M. R. H. White, *Nature*, 2010, **465**, 736–745.
9 F. M. Mickler, L. Möckl, N. Ruthardt, M. Ogris, E. Wagner and C. Bräuchle, *Nano Lett.*, 2012, **12**, 3417–3423.
10 A. Huefner, D. Septiadi, B. D. Wilts, I. I. Patel, W. L. Kuan, A. Fragniere, R. A. Barker and S. Mahajan, *Methods*, 2014, **68**, 354–363.

11 S. K. Mahto, T. H. Yoon and S. W. Rhee, *Biomicrofluidics*, 2010, **4**, 034111.
12 Y. Qiao, J. An and L. Ma, *Anal. Chem.*, 2013, **85**, 4107–4112.
13 P. M. Valencia, O. C. Farokhzad, R. Karnik and R. Langer, *Nat. Nanotechnol.*, 2012, **7**, 623–629.
14 J. Wu, Q. Chen, W. Liu and J.-M. Lin, *Lab Chip*, 2013, **13**, 1948–1954.
15 F. Sambale, F. Stahl, D. Bahnemann and T. Scheper, *J. Nanopart. Res.*, 2015, **17**, 298.
16 D. Huh, Y. S. Torisawa, G. A. Hamilton, H. J. Kim and D. E. Ingber, *Lab Chip*, 2012, **12**, 2156–2164.
17 A. Albanese, A. K. Lam, E. A. Sykes, J. V. Rocheleau and W. C. W. Chan, *Nat. Commun.*, 2013, **4**, 2718.
18 B. Kwak, A. Ozcelikkale, C. S. Shin, K. Park and B. Han, *J. Controlled Release*, 2014, **194**, 157–167.
19 M. B. Esch, G. J. Mahler, T. Stokor and M. L. Shuler, *Lab Chip*, 2014, **14**, 3081–3092.
20 D. Di Carlo, L. Y. Wu and L. P. Lee, *Lab Chip*, 2006, **6**, 1445–1449.
21 D. Wlodkowic, S. Faley, M. Zagnoni, J. P. Wikswo and J. M. Cooper, *Anal. Chem.*, 2009, **81**, 5517–5523.
22 S. Le Gac and A. van den Berg, *Trends Biotechnol.*, 2010, **28**, 55–62.
23 H. Yin and D. Marshall, *Curr. Opin. Biotechnol.*, 2012, **23**, 110–119.
24 J. El-Ali, P. K. Sorger and K. F. Jensen, *Nature*, 2006, **442**, 403–411.
25 M. A. Walling and J. R. E. Shepard, *Chem. Soc. Rev.*, 2011, **40**, 4049–4076.
26 S. T. Reddy, M. A. Swartz and J. A. Hubbell, *Trends Immunol.*, 2006, **27**, 573–579.
27 K. Murphy, P. Travers, M. Walport and C. Janeway, *Janeway's immunobiology*, Garland Science, New York, 8 edn, 2012.
28 L. E. Paulis, S. Mandal, M. Kreutz and C. G. Figdor, *Curr. Opin. Immunol.*, 2013, **25**, 389–395.
29 M. Zaman, M. F. Good and I. Toth, *Methods*, 2013, **60**, 226–231.
30 L. Xu, Y. Liu, Z. Chen, W. Li, Y. Liu, L. Wang, Y. Liu, X. Wu, Y. Ji, Y. Zhao, L. Ma, Y. Shao and C. Chen, *Nano Lett.*, 2012, **12**, 2003–2012.
31 P. J. Tacken, I. S. Zeelenberg, L. J. Cruz, M. A. van Hout-Kuijer, G. van de Glind, R. G. Fokkink, A. J. A. Lambeck and C. G. Figdor, *Blood*, 2011, **118**, 6836–6844.
32 A. McLintock, C. A. Cunha-Matos, M. Zagnoni, O. R. Millington and A. W. Wark, *ACS Nano*, 2014, **8**, 8600–8609.
33 C. J. Murphy, T. K. San, A. M. Gole, C. J. Orendorff, J. X. Gao, L. Gou, S. E. Hunyadi and T. Li, *J. Phys. Chem. B*, 2005, **109**, 13857–13870.
34 M. Junkin and S. Tay, *Lab Chip*, 2014, **14**, 1246–1260.
35 S. Mahmood, S. Nandagopal, I. Sow, F. Lin and S. K. P. Kung, *Eur. J. Immunol.*, 2014, **44**, 2737–2748.
36 N. Gopalakrishnan, R. Hannam, G. P. Casoni, D. Barriet, J. M. Ribe, M. Haug and O. Halaas, *Lab Chip*, 2015, **15**, 1481–1487.
37 S. Faley, K. Seale, J. Hughey, D. K. Schaffer, S. VanCompernolle, B. McKinney, F. Baudenbacher, D. Unutmaz and J. P. Wikswo, *Lab Chip*, 2008, **8**, 1700–1712.
38 I. Zaretsky, M. Polonsky, E. Shifrut, S. Reich-Zeliger, Y. E. Antebi, G. Aidelberg, N. Waysbort and N. Friedman, *Lab Chip*, 2012, **12**, 5007–5015.
39 B. Dura, S. K. Dougan, M. Barisa, M. M. Hoehl, C. T. Lo, H. L. Ploegh and J. Voldman, *Nat. Commun.*, 2015, **6**, 5940.
40 A. McLintock, N. Hunt and A. W. Wark, *Chem. Commun.*, 2011, **47**, 3757.
41 A. McLintock, H. J. Lee and A. W. Wark, *Phys. Chem. Chem. Phys.*, 2013, **15**, 18835–18843.
42 B. Nikoobakht and M. A. El-Sayed, *Chem. Mater.*, 2003, **15**, 1957–1962.
43 T. K. Sau and C. J. Murphy, *Langmuir*, 2004, **20**, 6414–6420.
44 A. Gole and C. J. Murphy, *Chem. Mater.*, 2005, **17**, 1325–1330.
45 M. B. Lutz, N. Kukutsch, A. L. J. Ogilvie, S. Rossner, F. Koch, N. Romani, G. Schuler and J. Immunol, *Methods*, 1999, **223**, 77–92.
46 I. Johnson, *The Molecular Probes Handbook: A Guide to Fluorescent Probes and Labeling Technologies*, Life Technologies Corporation, 11th edn, 2010.
47 L. Kim, Y.-C. Toh, J. Voldman and H. Yu, *Lab Chip*, 2007, **7**, 681–694.
48 B. B. Manshian, S. Munck, P. Agostinis, U. Himmelreich and S. J. Soenen, *Sci. Rep.*, 2015, **5**, 13890.
49 S. F. G. van Helden, F. N. van Leeuwen and C. G. Figdor, *Immunol. Lett.*, 2008, **117**, 191–197.
50 A. Badiee, V. Heravi Shargh, A. Khamesipour and M. R. Jaafari, *Vaccine*, 2013, **31**, 735–749.
51 M. A. Dobrovolskaia and S. E. McNeil, *Nat. Nanotechnol.*, 2007, **2**, 469–478.